UHBR OPEN-TEST-CASE FAN ECL5/CATANA, PART 2: MECHANICAL AND AEROELASTIC STABILITY ANALYSIS

Valdo Pagès, Pierre Duquesne, Stéphane Aubert, Laurent Blanc, Pascal Ferrand, Xavier Ottavy, Christoph Brandstetter

UHBR OPEN-TEST-CASE FAN ECL5/CATANA, PART 2: MECHANICAL AND AEROELASTIC STABILITY ANALYSIS

V. Pagès[1] - P. Duquesne[1] - S. Aubert[1] - L. Blanc[2]*
P. Ferrand[1] - X. Ottavy[1] - C. Brandstetter[1]

[1] Univ. Lyon, Ecole Centrale de Lyon, CNRS, Univ. Claude Bernard Lyon 1, INSA Lyon, LMFA, UMR5509, 69130, Ecully, France
[2] Univ. Lyon, Ecole Centrale de Lyon, CNRS, UMR5513, LTDS, 69130, Ecully, France
* valdo.pages@ec-lyon.fr

ABSTRACT

In Part-1, the ECL5 open-test-case has been introduced. Details on design methodology, geometry, and aerodynamics of the whole stage have been presented. Part-2 focuses herein on structure dynamics and aeroelastic stability. This paper aims to provide the mechanical and aeroelastic stability characteristics of the fan stage obtained with a state-of-art industrial design process.

The fan blades are composed of a laminate made of unidirectional carbon fibres and epoxy composite plies. Fibre orientations of each ply are parameters which enable to modify the mechanical behaviour with minimal impact on the aerodynamic performance. Details on the structural properties, the manufacturing process and the ply orientations are presented.

First mechanical modes of the fan are described and discussed in the context of aeroelastic interactions. Their frequency distribution is validated in terms of synchronous vibration. Aeroelastic stability of the fan is evaluated at representative operating points with a systematic approach. Potential instabilities are observed far from the operating line. Therefore, they do not compromise experimental campaigns.

KEYWORDS

FAN, COMPOSITE, AEROELASTIC, AEROACOUSTIC

NOMENCLATURE

E	Young's Elastic Modulus	f^s	Frequency in the steady frame
G	Shear Modulus	f^r	Frequency in the rotating frame
ν	Poisson's ratio	f^{cut}	Cut-off frequency
ζ	Aerodynamic damping	iNDj	Mode i at nodal diameter j
M	Mach number	UHBR	Ultra High Bypass Ratio
ρ	Density	OGV	Outlet Guide Vane
Ω	Rotation speed	EO	Engine Order

INTRODUCTION

Ultra High Bypass Ratio (UHBR) fan is a promising solution for the next decades to improve turbofans efficiency and to reduce the environmental impact of aeronautical propulsion. The high aspect ratio and the use of composite material for these fan blades induce new coupling problematics between aerodynamic, aeroelastic and aeroacoustic phenomena. In this context, a new open-test-case fan stage named ECL5 has been developed at Ecole Centrale de Lyon

(Brandstetter et al., 2021). In parallel, preliminary design has been used to develop flutter investigation methods (Duquesne et al. (2019b) and Rendu et al. (2020)). This open-test-case is provided to the turbomachinery community within the European CleanSky-2 project CATANA (Composite Aeroelastics and Aeroacoustics).

Since the 1990's, composite materials have been used in fans to achieve better performance. However composites were usually used in such configurations that quasiisotropic macro-properties appear. Recent research (Goerke et al. (2012) and Schmid et al. (2019)) showed that the use of anisotropic properties of composite could help to improve both mechanics and aerodynamics. Composites also present potential to control flutter by modification of eigenmodes according to (Reiber and Blocher, 2017). To be representative of the modern fan generations, the ECL5 fan is made of unidirectional carbon fibres and epoxy resine composite plies. Theses plies are stacked into a laminate with intentional ply orientations.

In this paper, the objective is to complete the fan description provided in Part-1 (Brandstetter et al., 2021) by focusing on structure and stability of the fan. To be representative of industrial configurations and to enable complete experimental campaigns, it is necessary that the fan presents stable operating conditions at every planned experimental rotation speed. First the composite structure of the fan resulting from the design process is described in detail. Then modeling strategies are presented. Finally, the dynamics of the fan are deducted and its aeroelastic stability is assessed.

ECL5 FAN COMPOSITE STRUCTURE

ECL5 fan (figure 1) is made up of 16 blades. The fan blade geometry is detailed in Part-1. The main characteristics are presented in table 1. The blade is exclusively made of unidirectional carbon fibres and epoxy composite plies. A ply is considered to be made of orthotropic material. The three material orthotropy directions are defined locally as follows : direction 1 is the orientation of the carbon fibres, direction 2 is orthogonal to direction 1 within the ply and direction 3 is orthogonal to the ply. The constitutive law of the composite material is described classically by nine constants listed in table 2 (indicated by composite manufacturer).

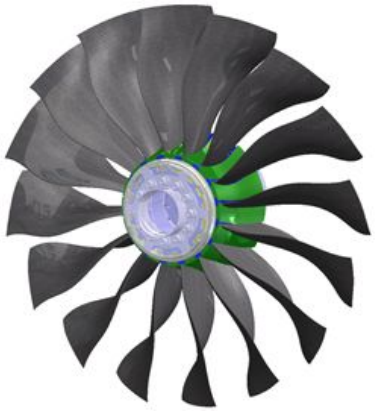

Figure 1: ECL5 fan

Number of blades	16
Diameter	$508\ \mathrm{mm}$
Design speed	11000 rpm
Design massflow	$36.0\ \mathrm{kg/s}$
Design pressure ratio	1.35
Design M^r_{tip}	1.0

Table 1: ECL5 parameters

ρ	E_1	$E_2 = E_3$	G_{23}	$G_{12} = G_{13}$	ν_{23}	$\nu_{12} = \nu_{13}$
$1560\ \mathrm{kg/m^3}$	123.0 GPa	9.3 GPa	5.0 GPa	4.5 GPa	0.3	0.26

Table 2: Material properties

The maximal thickness of the blade (at the root) is $13.3\ \mathrm{mm}$. The thickness of a ply is

Ply	1	2	3	4	5	6	7	8	9
Orientation	$45°$	$-45°$	$-15°$	$-30°$	$15°$	$-15°$	$70°$	$0°$	$0°$
Ply	10	11	12	13	14	15	16	17	18
Orientation	$-15°$	$0°$	$0°$	$60°$	$-60°$	$0°$	$0°$	$60°$	$-60°$

Table 3: Blade plies orientation

0.15 mm so the maximum number of plies is 88. The internal structure is symmetric with respect to the laminate midplane to minimize the coupling of in-plane and out-of-plane movement. Each point of the midplane is associated with a number of plies defined by the blade local thickness. Plies are ranked by their size (see figure 2).

For the design process, plies have been divided in two families. The 18 largest plies are called blade plies and the others - the smallest - are called core plies. To reduce the number of degrees of freedom for the design, orientation of core plies is set to $0°$, defined as the radial direction. Indeed their influence on global elastic properties is minor and they mainly contribute in thickness adjustment. Thus the total number of fibre orientations to define is set to 18. These orientations are listed in table 3. The orientation of a ply is defined as illustrated in figure 2b. The orientation is imposed on a chosen point at the root of the blade. Local orientation along the blade is determined by the draping of the surface (Wang et al. (1999)).

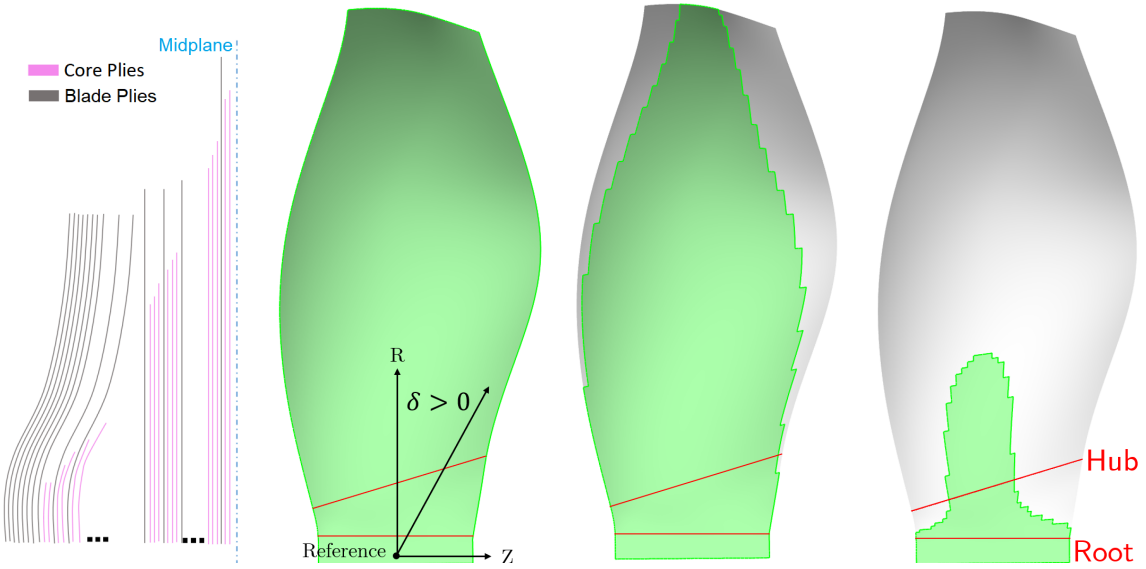

(a) Ply alternation (b) Ply 1 (blade): wrap (c) Ply 6 (blade) (d) Ply 19 (core)

Figure 2: Plies of ECL5 Fan (colored in green)

The manufacturing process consists of three steps. First, each pre-impregnated ply is cut to the pre-defined shape. Secondly, the plies are stacked into two half-molds. Then both molds are pressed together before heating to start polymerisation process of epoxy.

The plies are stacked in a particular way to improve the manufacturing process. It is made of an alternation of blade plies and core plies as illustrated in figure 2a. The detailed stacking sequence will be detailed under catana.ec-lyon.fr. One particular feature is that Ply 1 (the largest) is put at the external surface of the blade. Thus, the external surface is composed of only one ply and has a very low surface roughness without any sharp step.

MODELLING STRATEGY FOR MECHANICAL AND AEROELASTIC ANALYSIS

Mechanical simulations

Mechanical simulations are realized with a finite element (FEM) solver (Ansys[1]). The simulation domain and boundary conditions are presented in figure 3a. A cyclic symmetry condition is imposed on the faces of the disk sector (in purple) since fan is supposed to be tuned and all blades identical. The shaft of the test facility is not modeled. To represent the contact between the disk and the shaft, the disk is clamped in the blue area and the axial displacement is set to zero in the green area. The aerodynamic pressure field is imposed on the red surface. Static simulations include non-linear deformation. The contact between the disk and the blade is modeled with a friction coefficient of 0.1 (indicated by composite manufacturer) with an Augmented Lagrange formulation (Kannan and Kramer, 1994) which enables penetration for static simulations. For modal simulations, it is clamped.

The blade composite laminate is modelled by a hexaedric 3D mesh (Ansys[2]) and dedicated procedure to model the plies alternation. To reduce the mesh size, a stack of plies is modelled with a representative element. Each half-thickness is modelled by a single element (see figure 3b) whose orthotropic properties are homogenized from classical laminate theory (Barbero, 2013).

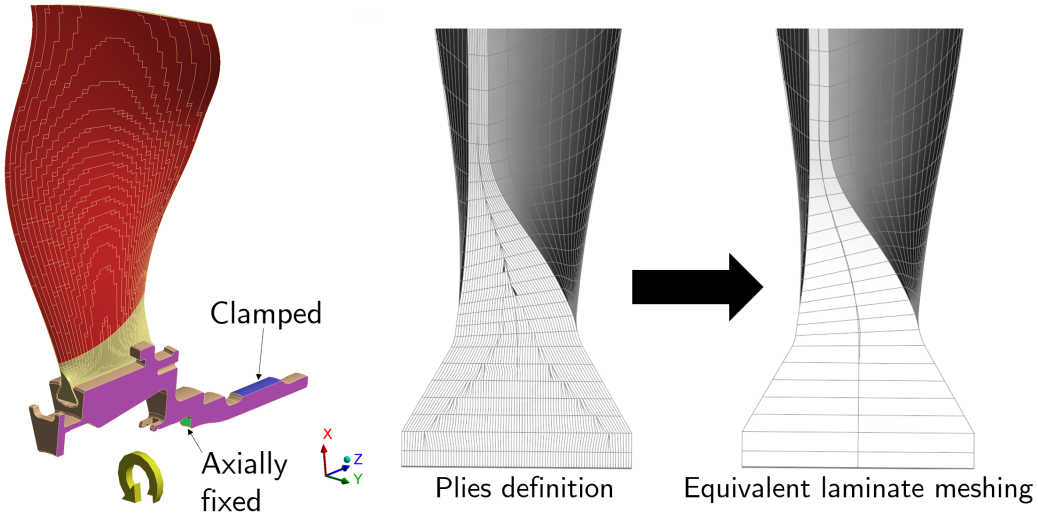

(a) Boundary conditions (b) Blade thickness meshing

Figure 3: Mechanical model

Aeroelasticity

The isolated fan is considered for the stability study. It is common practice for fan flutter studies based on self-excitation (Sanders et al. (2004), Aotsuka and Murooka (2014), Vahdati and Cumpsty (2015)). The OGV is one chord distant downstream of the fan so its potential influence is significantly reduced.

Aeroelastic stability is typically investigated with the so-called energy method according to Carta (1967). The basic assumption is that unsteady aerodynamic forces do not change the structural dynamics of the aeroelastic system. Thus eigenmodes and natural frequencies can be determined once and for all.

[1]https://www.ansys.com/products/structures/ansys-mechanical
[2]https://www.ansys.com/products/structures/composite-materials

Numerical flutter analysis is thereafter performed by computing the harmonic pressure variation on the surface of the blades. These unsteady loads lead to a certain amount of aerodynamic work per cycle W. A negative work entry ($W < 0$) indicates that energy is transferred from the fluid into the structure, thus exciting the blade vibration and leading to aeroelastic instability. For a positive entry ($W > 0$), the blade releases energy to the fluid so that vibrations are damped. The aerodynamic damping value can be stated as :

$$\zeta = \frac{W}{4\pi E_k} = \frac{W}{2\pi M_0 \omega_0^2} \tag{1}$$

with the modal kinetic energy E_k of the travelling wave, the modal mass M_0 and vibration angular frequency ω_0.

Time-linearised simulations

To assess the stability of the fan, a time-linearized method (LRANS) is used. Based on the assumption of small harmonic perturbations, the coordinates of the grid vertices as well as the flow solution can be decomposed in a steady part and a time dependent harmonic perturbation. These two parts are simulated separately.

The steady flow is obtained with the compressible RANS solver elsA (Gazaix et al., 2002). The solver relies on cell-centered finite volume method on multi-block structured grids. Convective flows are obtained with Jameson scheme with artificial dissipation. The turbulence is modeled by $k-\omega$ Kok model with vorticity-based computation of turbulent kinetic energy production. A single passage of the fan domain contains 2.3 Million cells, with 101 layers in radial direction. 21 layers are used in the tip gap. The wall resolution of this mesh is below y+ = 1 for design conditions. Comparison of steady states described in Part-1 was carried out and showed few disparities, resulting in differences lower than 0.3% in total pressure ratio and 0.3% in isentropic efficiency for the studied operation points.

The linearized flow is obtained with the solver Turb'Lin (Rendu et al., 2015). The solution is obtained in the frequency domain. This vertex-centered LRANS solver has been validated for transonic separated flows by Philit et al. (2012) and Rendu et al. (2015). The turbulence model has been linearized (see Duquesne et al. (2018) for comparison of results with frozen turbulence assumption). Upstream and downstream of the fan, the mesh was extended by numerous rotor diameters with strongly reduced axial resolution to attenuate acoustic reflections.

RESULTS

Mechanics

Static mechanics

Hot shapes of the fan blade were determined for each speedline along the working line. Due to the use of anisotropic properties of composite, the maximal blade displacement is $1.15\ \mathrm{mm}$ at maximal speed corresponding to 1.0% of the chord. It is comparable to the optimization realized by Schmid et al. (2019). Hot shapes will be provided under catana.ec-lyon.fr.

Mode Shapes

Concerning synchronous excitation phenomena, intake distortions are the predominant sources. The potential effects of the OGV are negligible because of the axial distance from the fan, of more than one chord. Experience on similar configurations (Brandstetter et al. (2019) and Rodrigues et al. (2020)) shows that above the 6^{th} engine order, forced response amplitudes

are negligible. At 105% rotation speed, the 6^{th} engine order frequency is 1155 Hz. Mode 3 and Mode 4 frequencies are respectively around 900 Hz and 1500 Hz at maximal rotation speed so only the first three modes are considered in the following.

Modal data in the following are presented only for positive nodal diameters because they're identical for both co-rotative and contra-rotative modes. Modal frequencies are given in figure 4a for each nodal diameter (ND). Frequency variations are less than 2% except for low nodal diameters between modes of the same family. Mode 1ND0 frequency is lowered by 9% compared to the other NDs. Mode 2ND1 and Mode 3ND1 frequencies are also reduced by respectively 12% and 14%. To assess for mode shape variations between nodal diameters, the Mode Assurance Criterion (MAC) is used (Allemang, 2003). For each mode, the mode shape is compared to its ND8 counterpart. MAC is equal to 1 if the mode shapes are identical, 0 if they are inconsistent. MAC is represented in figure 4b. Modes 2ND1 and 3ND1 are very different from other NDs. Mode 1ND0 mode shape is comparable even if its frequency is slightly different. These significant variations between nodal diameters have to be taken into account for aeroelastic studies.

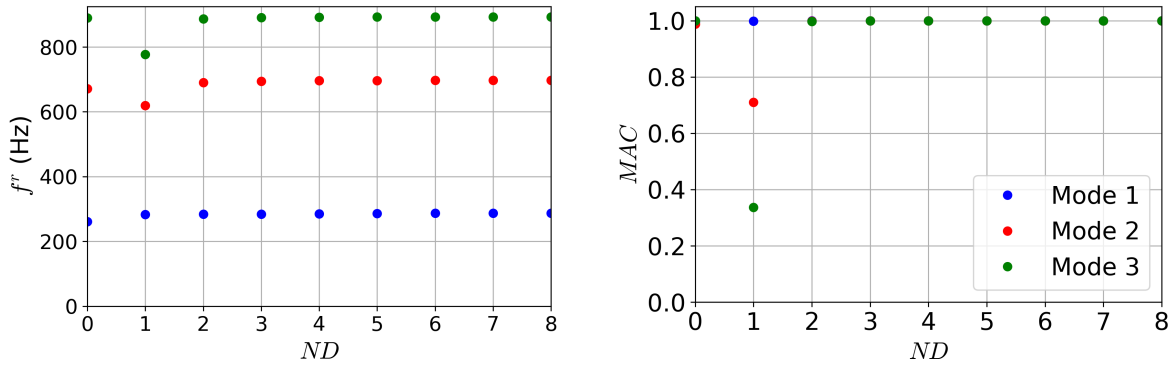

(a) Frequency

(b) MAC in comparison with ND8

Figure 4: Nodal diameter influence on modes at 100% speed

Mode shapes at ND2 are shown in figure 5. ND2 is representative of all nodal diameters except ND1. Mode 1 is a bending mode with very low torsional component. The displacement is almost only circumferential without axial component. Mode 2 shows a pronounced torsional component at the blade tip which is known to be critical for fluid-structural interactions (Duquesne et al. (2019a) and Stapelfeldt and Brandstetter (2020)). Mode 3 represents a torsional mode with torsional center positioned at half-chord at midspan and at the leading edge at the tip.

Mode shapes at ND1 are shown in figure 6. As identified in figure 4b, Mode 2ND1 and Mode 3ND1 are very different from their other equivalent NDs. In particular, the mode shape of 3ND1 is closer to Mode 2 than Mode 3. It can be inferred that the disk influence for this nodal diameter is very high. Furthermore the accuracy of the prediction can be affected by support stiffness and gyroscopic effects. Thus the choice to model the disk without the shaft could have an important impact on this nodal diameter and must be addressed in further studies.

Campbell diagram

The campbell diagram obtained of the fan is presented in figure 7. The crossings of the different modes are highlighted. These are sufficiently distributed in frequency to enable tests

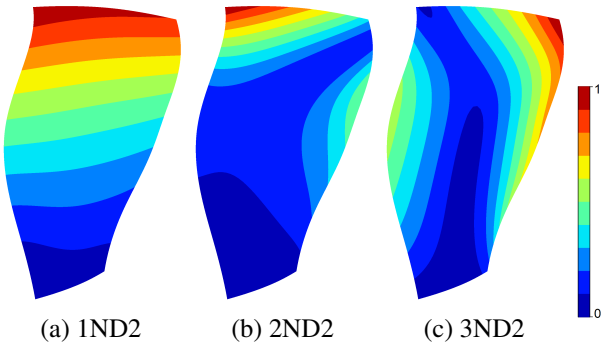

(a) 1ND2 (b) 2ND2 (c) 3ND2

Figure 5: Normalized modal displacement amplitude at ND2

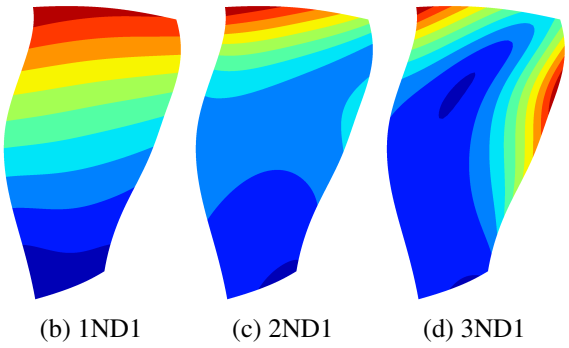

(b) 1ND1 (c) 2ND1 (d) 3ND1

Figure 6: Normalized modal displacement amplitude at ND1

at low part-speed (50%), high part-speed (80%) and full speed (100% and above). Experience shows that the predicted frequencies are systematically slightly higher than those of manufactured blades. Fans produced by the same manufacturer (Brandstetter et al. (2019) and Rodrigues et al. (2020)) show that the frequency predictions are nearly 5% higher for torsional modes. Moreover, in previous experimental campaigns, crossing with engines orders higher than 3 never prevented speedline exploration. Hence, the 80% speedline can be safely investigated if the frequency of Mode 3 will be slightly lower than predicted.

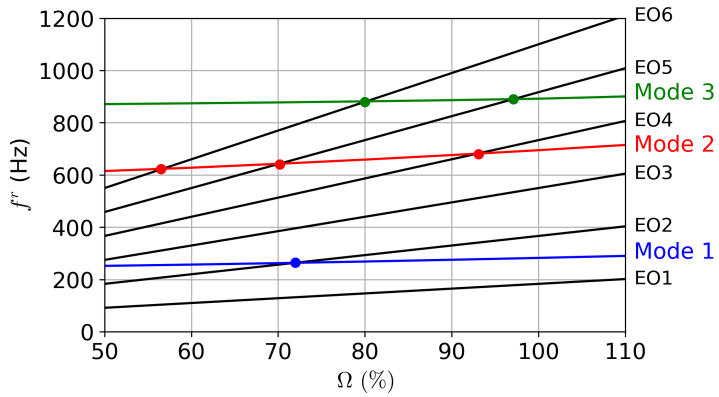

Figure 7: Campbell diagram at ND2

Overall stability analysis

Strategy

To be representative of industrial configurations and to enable comprehensive experimental campaigns, it is necessary that the fan presents stable operating conditions at every planned experimental rotation speed. An exhaustive review would be to test every nodal diameter of every mode at each rotation speed. Even with LRANS method, this exceeds the scope of a design study. In this paper, five operating points representative of the different flow limits are presented. These points are represented on the compressor map showed in figure 8. OP-A is the design point at 100% speed. The flow is transonic without separations. It serves as reference and must be stable in any case. OP-B is the maximum pressure ratio at 100% speed. The shock on the suction side produces a boundary layer separation. OP-C presents a choked flow with a separation downstream of the shock. OP-D and OP-E are operating points near the maximum

pressure ratio at 80% speed. The flow is subsonic and characterized by a leading edge flow separation. It is to notice that at part speed, choke occurs in the OGV before the fan. More details about the flow of these operating points can be found in Part-1.

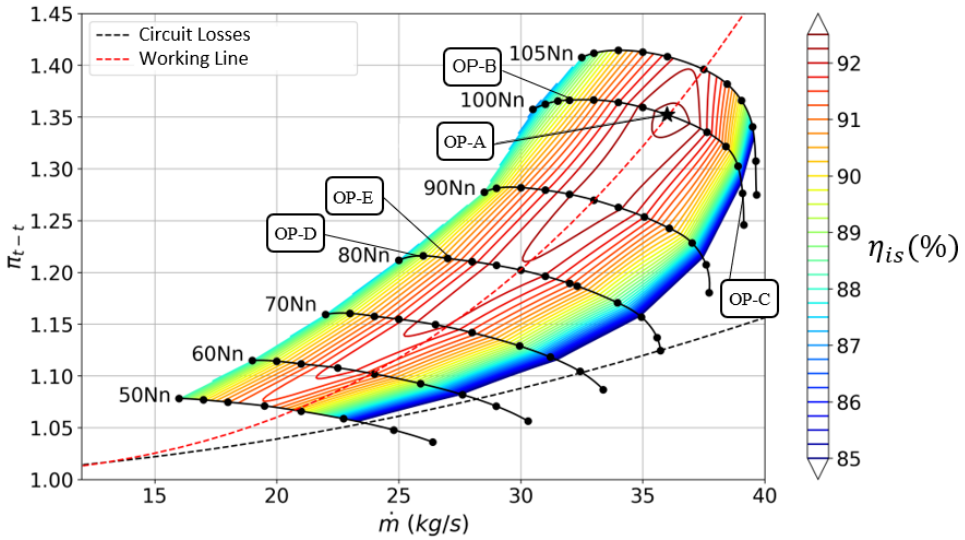

Figure 8: Compressor map with stability point of interest

Flutter events detected on modern fans mostly involve first bending mode at low nodal diameter (Sanders et al. (2004), Aotsuka and Murooka (2014), Vahdati and Cumpsty (2015)). However it has been shown by Stapelfeldt and Brandstetter (2020) that torsional mode shapes could lead to aeroelastic instability for a convective mechanism denoted as Non-Synchronous Vibration. Thus all three modes were investigated. Table 4 gives tip reduced frequencies based on chord and upstream relative velocity at both considered speeds.

To reduce the number of aeroelastic configurations to simulate, only even numbers of nodal diameters were simulated in a first step. The nodal diameters ± 1 were added because their aeroelastic behaviour can't be deduced from other nodal diameters due to their mode shape (see figures 5 and 6). Odd nodal diameters were simulated if discontinuities in aerodynamic damping curves were observed.

Aerodynamic damping

Figures 9a to 9d show the aerodynamic damping ratio ζ as function of the nodal diameter operating points OP-A to OP-D. OP-E will be detailed separately in the following. The minimal value of each curve are gathered in table 5. At OP-A, the design point, it is always positive and the minimal value reached is 1.38%. Mode 1 aerodamping variations as function of nodal diameter are smooth for every operating point. Smallest values occurs between ND0 and ND2 and exceeds 5% for high NDs. For every operating point studied, Mode 1 is globally more stable than Mode 2 or Mode 3, especially at high NDs. Aerodamping curves for Mode 2 and Mode 3 are more erratic and minimal values are reached for various NDs. Only one point was found to be unstable : Mode 2ND5 at OP-D. Among all other simulated configurations, the aerodamping is always higher than 0.69%.

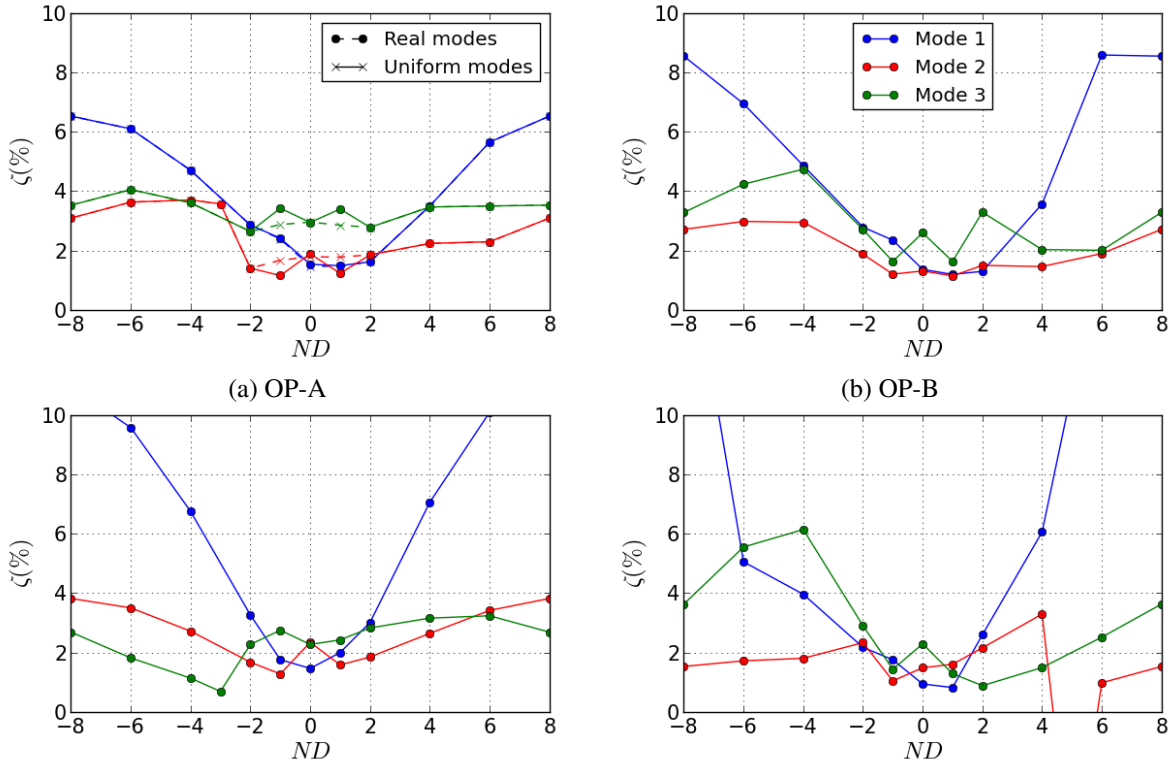

(a) OP-A

(b) OP-B

(c) OP-C

(d) OP-D

Figure 9: Aerodynamic damping as function of nodal diameter

Speedline	80%	100%
Mode 1	0.09	0.08
Mode 2	0.22	0.19
Mode 3	0.30	0.24

Table 4: Reduced frequency on working line (ND8)

Operating point	Mode 1	Mode 2	Mode 3
OP-A (100%, 36.0 kg/s)	1.50%	1.38%	1.84%
OP-B (100%, 32.0 kg/s)	1.20%	1.15%	1.64%
OP-C (100%, 38.9 kg/s)	1.47%	1.28%	0.69%
OP-D (80%, 26.0 kg/s)	0.83%	−5.60%	0.89%

Table 5: Minimum of aerodamping

Influence of mode frequency and mode shapes on damping

Abrupt changes are observed in damping curves. Among possible reasons, one could be the change of mode shape and frequency for low nodal diameters (figure 4). This dependency was quantified at OP-A. Aerodynamic damping is computed with the same frequency and mode shape from ND8 (Uniform modes) which is similar to ND2 shown figure 5. It is compared to aerodynamic damping obtained with modes from FEM (Real modes) on figure 9a. Resulting curves with uniform modes are smoother. Aerodamping is mostly impacted at for mode $2\text{ND}\pm1$ and mode $3\text{ND} \pm 1$ whose modal shapes and frequencies were very different of other NDs. Mode 1ND0 has a shift in frequency of 9%, however the impact on the stability behavior is marginal. Then erratic changes observed between nodal diameters -2 and 2 are mostly due to mode shapes variations.

Instability analysis

Upstream and downstream acoustic conditions can produce discontinuities in stability behaviour of the blades (Ferria et al., 2012). On the operating points studied, numerous switches

of cut-on/cut-off conditions can be observed but only three discontinuities related to acoustic behaviour that could lead to instability were identified :

- For Mode 2ND-3 at OP-A, the stability curve is flat at each side of the discontinuity and the fan remains stable.
- For Mode 3ND-3 at OP-C, the stability reaches a minimum but the fan remains stable.
- For Mode 2ND5 at OP-D, the fan is predicted unstable and the aerodamping reaches a negative minimum at $\zeta = -5.6\%$. The stability behaviour for ND4 to ND6 is investigated in the following.

Aeroelastic instability of Mode 2 at OP-D

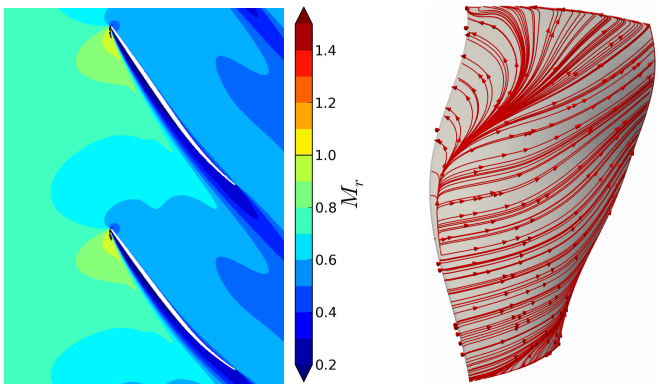

(a) Mach number at 90%H (b) Friction lines

Figure 10: Steady flow at OP-D

Figure 10 shows the steady flow at OP-D. The flow is subsonic and characterized by a thick boundary layer at suction side. Boundary layer separation occurs at the leading edge. It extends up to 35% of the chord, based on friction lines.

For Mode 2ND5 at this operating point, the fan is predicted unstable and the aerodamping reaches a negative minimum at $\zeta = -5.6\%$. The local work at the surface of the blade, normalized like the global work by $U = 4\pi E_k$ (see equation 1), is plotted figure 11 for ND4 to ND6. The local work is mostly located at the tip of the blade because of the mode shape (see figure 5b). Corresponding flow fluctuations at ND5 are more than one order of magnitude higher than for adjacent nodal diameters. For example, if the displacement is arbitrary set to 1.0% of the chord at the tip, the maximal pressure fluctuations will be 65% of inlet static pressure. At ND5, fluctuations can't be analyzed quantitatively because it is out of the hypothesis of small perturbations on which the linearized method is based.

At ND4 and ND6, the hypothesis of small perturbations remains valid and the work distribution can be analysed. Figure 11 shows that both suction side and pressure side are equivalently involved in overall stability of the blade. The local work patterns between ND4 and ND6 on the pressure side are similar but of opposite sign. On the pressure side, patterns are different. At ND4, the work is negative and positive near the leading edge with high values. Whereas the work is mildly positive at ND6 on a large area. This important change of behaviour between these nodal diameters indicates resonance, which is reached near ND5. Damping value obtained at ND5 is questionable due to resonance. However it still shows that instability could be expected at these operating conditions which must be investigated with caution during experiments.

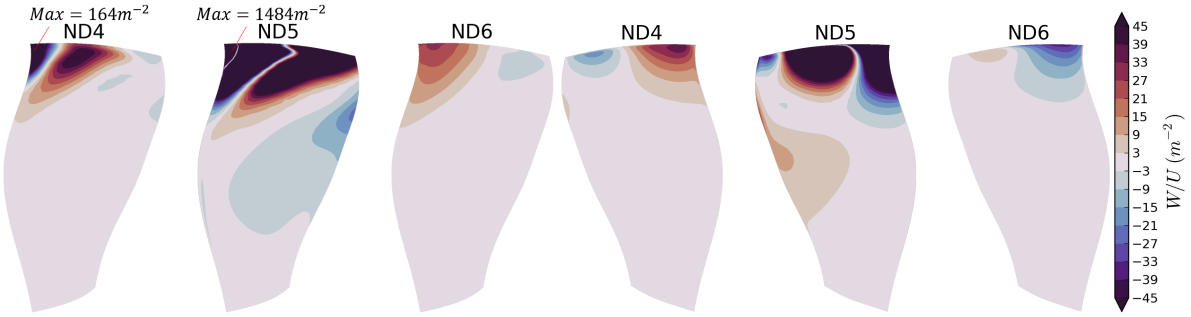

(a) Suction side (b) Pressure side

Figure 11: Local work at OP-D for Modes 2ND4 to 2ND6

Acoustic propagation conditions

The propagation conditions (Hellmich and Seume, 2008) of Mode 2 at OP-D are presented in figure 12. This figure gives an understanding of the acoustics in the duct. An acoustic pressure wave generated by a vibrating fan can propagate axially if the frequency in the steady frame of reference f^s is higher than a frequency f^{cut} called cut-off frequency. f^s is determined by the following equation :

$$f^s = |f^r + \Omega\,\mathrm{ND}| \tag{2}$$

with f^r the frequency in the rotating frame of reference (i.e. the modal frequency). On the assumption of uniform flow in radial direction, rigid body flow and hard-walled duct, the acoustic cut-off frequency for a subsonic axial flow can be estimated according to Hellmich and Seume (2008) as :

$$f^{cut} = \frac{k_r a}{2\pi} * \left(\sqrt{1 - M_x^2} \pm M_\theta\right) \tag{3}$$

with M_x and M_θ the axial and circumferential Mach number, a the sound speed and k_r the radial modal wave number calculated from Bessel functions. M_x and M_θ are determined by the mean value far upstream and downstream of the blade. Propagation conditions are shown in figure 12 and are verified in the linearized simulations. Upstream, acoustic waves propagate for ND4 to ND6. Downstream, acoustic waves propagate at ND4 but neither ND5 nor ND6. Vibration patterns which fulfill this condition of being cut-on only in one axial direction are known to be critical for aeroelastic stability (Atassi et al. (1995) and Fiquet et al. (2020)). Both discontinuities observed in the aerodamping curve (fig. 13) for OP-D coincide with changes of the acoustic propagation conditions (ND1 and ND5) shown in fig. 12.

Influence of operating point

Aeroelastic stability is compared between OP-D and OP-E for Modes 2ND4 to 2ND6. At OP-E, the massflow is 3.8% higher than at OP-D and the leading edge separation size is reduced to 25% of the chord. The acoustic propagation conditions upstream and downstream at OP-E for ND4 to ND6 are the same as at OP-D. The normalized local work distribution are presented in figure 14. Contrary to OP-D (figure 11), results show very little influence of the nodal diameter at this operating point and only stabilizing aerodynamic damping higher than 2.0% (see figure 13). On the suction side, the work repartition looks like ND4 at OP-D but with lower amplitude (see figure 11). Unlike results at OP-D, the work on the pressure side is one order lower than on suction side. Here, the stability of the blade is driven by the suction side. The shift of 3.8%

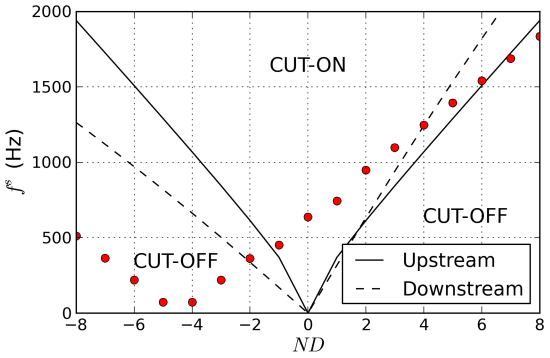

Figure 12: Mode 2 acoustic conditions at OP-D and OP-E

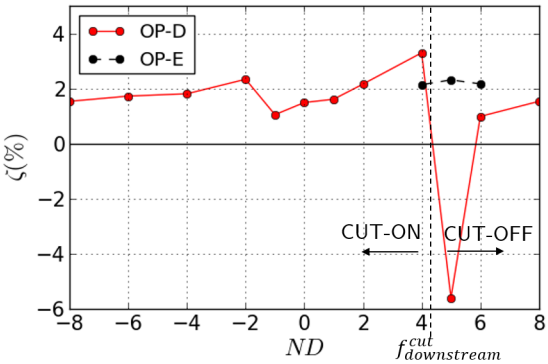

Figure 13: Influence of operating point

in massflow leads to a stable system and suppress the strong influence of nodal diameter on fan stability. Thus, even if the acoustic conditions are similar, the fan remains stable closer to the operating line. Based on the presented study it is not clear if the acoustic conditions are the dominant driver for instability or if a convective mechanism as described by Stapelfeldt and Brandstetter (2020) leads to aeroelastic lock-in. The latter case is not improbable as the five nodal diameter pattern can be in resonance with a backward travelling aerodynamic disturbance of wave-number 11 (aliased on a 16 bladed rotor). This disturbance would propagate with a speed of 59% of the rotor speed in the absolute frame of reference which is well in the range of reported convective disturbances (Rodrigues et al. (2020)) but has not been investigated before using time-linearized methods. Nevertheless, the detected instability at OP-D doesn't prevent experimental exploitation of the speedline as it occurs only close to the stall limit and in case of convective lock-in limit cycle oscillations are expected.

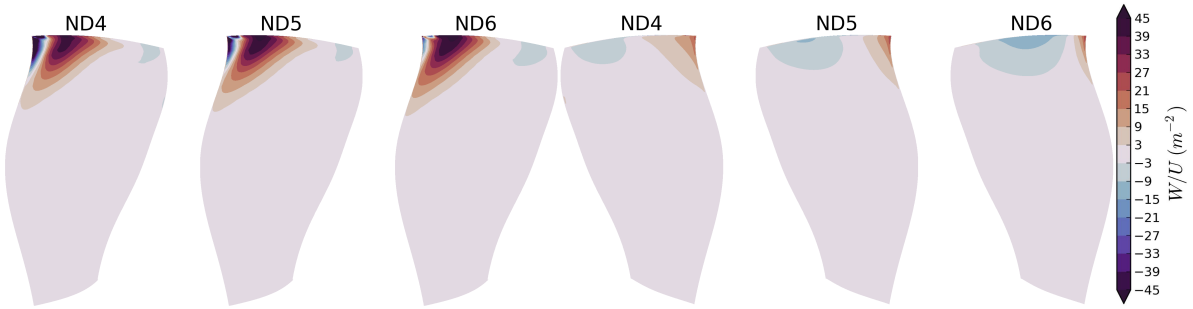

(a) Suction side (b) Pressure side

Figure 14: Local work OP-E for Modes 2ND4 to 2ND6

CONCLUSION

A fan representative of modern UHBR fans was designed and is established as a open-test case. The fan blades are made of unidirectional carbon fibres and epoxy composite plies. To enable an analysis of the dynamic behaviour, structural properties, manufacturing process and ply orientations were presented.

The second mode of the fan has a pronounced torsional component at the blade tip which makes it likely to be critical for fluid-structural interactions. Modes of a same family vary significantly at low nodal diameters. The impact of this disparity was quantified in aeroelastic studies. Fan stability was systematically investigated over representative operating points with

a time-linearized method. At nominal speed, no aeroelastic instabilities were detected. Thus it will be possible to investigate highly loaded operating conditions. At part-speed, a potential instability area was observed and will be investigated in more details in future work. It was shown that the instability area remains located far from the operating line and will be in the focus of the planned experimental campaign.

ACKNOWLEDGEMENTS

The present work has been supported by CIRT (Consortium Industrie-Recherche en Turbomachine). CATANA has received funding from the Clean Sky 2 Joint Undertaking (JU) under grant agreement $N°864719$. The JU receives support from the European Union's Horizon 2020 research and innovation program and the Clean Sky 2 JU members other than the Union. This publication reflects only the author's view and the JU is not responsible for any use that may be made of the information it contains. The authors thank the continuous support of Safran Aircraft Engines, and particularly the contribution of Laurent Jablonski during the design phase of the Open-Test-Case.

REFERENCES

Allemang, R. J. (2003). The modal assurance criterion - twenty years of use and abuse. *Sound and Vibration*, page 8.

Aotsuka, M. and Murooka, T. (2014). Numerical Analysis of Fan Transonic Stall Flutter. In *Proceedings of the ASME Turbo Expo 2014: Turbine Technical Conference and Exposition. Volume 7B: Structures and Dynamics.*, volume V07BT35A020, Dusseldorf, Germany. ASME.

Atassi, H. M., Fang, J., and Ferrand, P. (1995). Acoustic blockage effects in unsteady transonic nozzle and cascade flows. In *33rd Aerospace Sciences Meeting and Exhibit*, volume 95-0303, page 9, Reno, NV. AIAA.

Barbero, E. J. (2013). *Finite Element Analysis of Composite Materials Using ANSYS, Second Edition*. CRC Press.

Brandstetter, C., Pages, V., Duquesne, P., Ottavy, X., Ferrand, P., Aubert, S., and Laurent, B. (2021). UHBR Open-Test Case Fan ECL5/CATANA, Part 1 : Geometry and aerodynamic performance. In *14th European Conference on Turbomachinery Fluid dynamics and Thermodynamics*, Gdansk, Poland.

Brandstetter, C., Paoletti, B., and Ottavy, X. (2019). Compressible Modal Instability Onset in an Aerodynamically Mistuned Transonic Fan. *Journal of Turbomachinery*, 141(3): 031004:13.

Carta, F. O. (1967). Coupled Blade-Disk-Shroud Flutter Instabilities in Turbojet Engine Rotors. *Journal of Engineering for Power*, 89(3):419–426.

Duquesne, P., Aubert, S., Rendu, Q., and Ferrand, P. (2018). Effect of nodal diameter on the local blades vibration on the choke flutter instability in transonic UHBR fan. In *The 15th International Symposium on Unsteady Aerodynamics, Aeroacoustics and Aeroelasticity of Turbomachines*, Oxford, UK.

Duquesne, P., Mahieux, B., Aubert, S., and Ferrand, P. (2019a). Sensitivity of the aerodynamics damping coefficient prediction to the turbulence modelling conjugated with the vibration mode shape. In *Proceedings of 13th European Conference on Turbomachinery Fluid dynamics & Thermodynamics*, Lausanne, Switzerland.

Duquesne, P., Rendu, Q., Aubert, S., and Ferrand, P. (2019b). Choke flutter instability sources tracking with linearized calculations. *International Journal of Numerical Methods for Heat & Fluid Flow*, 30(9):4155–4166.

Ferria, H., Ferrand, P., Pacull, F., and Aubert, S. (2012). Numerical investigation of flutter stability in subsonic space turbine blisk with emphasis on cut-on/cut-off modes and interblade phase angles. *Journal of Thermal Science*, 21(6):492–499.

Fiquet, A.-L., Vercoutter, A., Buffaz, N., Aubert, S., and Brandstetter, C. (2020). Acoustic resonance in an axial multistage compressor leading to non-synchronous blade vibration. In *Proceedings of Proceedings of ASME Turbo Expo 2020 & Turbomachinery Technical Conference and Exposition*, London, UK. ASME.

Gazaix, M., Jollès, A., and Lazareff, M. (2002). The elsA object-oriented computational tool for industrial applications. *ONERA-Publications-TP*, 220.

Goerke, D., Le Denmat, A.-L., Schmidt, T., Kocian, F., and Nicke, E. (2012). Aerodynamic and Mechanical Optimization of CF/PEEK Blades of a Counter Rotating Fan. In *ASME Turbo Expo 2012: Turbine Technical Conference and Exposition. Volume 7: Structures and Dynamics, Parts A and B*, pages 21–33, Copenhagen, Denmark. ASME.

Hellmich, B. and Seume, J. R. (2008). Causes of Acoustic Resonance in a High-Speed Axial Compressor. *Journal of Turbomachinery*, 130(3):031003.

Kannan, B. K. and Kramer, S. N. (1994). An Augmented Lagrange Multiplier Based Method for Mixed Integer Discrete Continuous Optimization and Its Applications to Mechanical Design. *Journal of Mechanical Design*, 116(2):405–411.

Philit, M., Ferrand, P., Labit, S., Chassaing, J.-C., Aubert, S., and Fransson, T. (2012). Derivated Turbulence Model to Predict Harmonic Loads in Transonic Separated Flows over a Bump. In *28th International Congress of the Aeroanautical Sciences*, page 11, Brisbane, Australia. ICAS.

Reiber, C. and Blocher, M. (2017). Potential of aeroelastic tailoring to improve flutter stability of turbomachinery compressor blades. In *Proceedings of 12th European Conference on Turbomachinery Fluid dynamics & Thermodynamics*, page 10, Stockholm, Sweden.

Rendu, Q., Aubert, S., and Ferrand, P. (2020). Numerical identification of mechanisms triggering 2D choke flutter in transonic fan. *Journal of Fluids and Structures*, 97:102879.

Rendu, Q., Philit, M., Rozenberg, Y., Labit, S., and Chassaing, J.-C. (2015). Time-linearized and harmonic balance navier-stokes computations of a transonic flow over an oscillating bump. page 14, Stockholm, Sweden.

Rodrigues, M., Soulat, L., Paoletti, B., Ottavy, X., and Brandstetter, C. (2020). Aerodynamic investigation of a composite low-speed fan for uhbr application. In *Proceedings of Proceedings of ASME Turbo Expo 2020 & Turbomachinery Technical Conference and Exposition*, page 13, London, UK. ASME.

Sanders, A. J., Hassan, K. K., and Rabe, D. C. (2004). Experimental and Numerical Study of Stall Flutter in a Transonic Low-Aspect Ratio Fan Blisk. *Journal of Turbomachinery*, 126(1):166–174.

Schmid, T., Lengyel-Kampmann, T., Schimdt, T., and Nicke, E. (2019). Optimization of a carbon fiber composite blade of a counter-rotating fan for aircraft engines. In *Proceedings of 13th European Conference on Turbomachinery Fluid dynamics & Thermodynamics*, Lausanne, Switzerland.

Stapelfeldt, S. and Brandstetter, C. (2020). Non-synchronous vibration in axial compressors: lock-in mechanism and semi-analytical model. *Journal of Sound and Vibration*, 488:115649.

Vahdati, M. and Cumpsty, N. (2015). Aeroelastic Instability in Transonic Fans. *Journal of Engineering for Gas Turbines and Power*, 138(2):022604.

Wang, J., Paton, R., and Page, J. R. (1999). The draping of woven fabric preforms and prepregs for production of polymer composite components. *Composites Part A: Applied Science and Manufacturing*, 30(6):757–765.